CARBON 94 (2015) 455–463

Contents lists available at ScienceDirect

CARBON

journal homepage: www.elsevier.com/locate/carbon

# Defect-engineered mesoporous ternary nanoarchitecture of zinc-cobalt-oxide/nitrogen-doped graphene as anode material in lithium ion batteries

Sumanta Sahoo [a,1], Seok-Hu Bae [a,1], Yun-Sung Lee [b], Jung-Min Lee [c], Joon-Mo Ahn [c], Chun-Gon Kim [d], Il-Kwon Oh [a,*]

[a] Graphene Research Center, KAIST Institute for the Nano Century, Department of Mechanical Engineering, School of Mechanical and Aerospace Engineering, Korea Advanced Institute of Science and Technology, 291 Daehak-ro, Yuseong-gu, Daejeon 305-701, Republic of Korea
[b] Faculty of Applied Chemical Engineering, Chonnam National University, Gwang-ju 500-757, Republic of Korea
[c] Agency for Defense Development, Yuseong P.O. Box 35-44, Daejeon 305-600, Republic of Korea
[d] Department of Aerospace Engineering, KAIST, 373-1 Guseong-dong, Yuseong-gu, Daejeon 305-701, Republic of Korea

ARTICLE INFO

*Article history:*
Received 13 May 2015
Received in revised form 4 July 2015
Accepted 6 July 2015
Available online 7 July 2015

ABSTRACT

We report a defect-engineered self-assembly route to a mesoporous ternary $ZnCo_2O_4$/nitrogen-doped graphene nanoarchitecture as an anode material for lithium ion batteries through a hydrothermal and thermal annealing process. A hetero-nanostructure showed flower-like $ZnCo_2O_4$ nanosheets which were well dispersed and firmly decorated on nitrogen-doped reduced graphene oxide, as atomic-scale defects such as nitrogen-doped sites and oxygen-functional groups in chemically modified graphene oxide can be more reactive nucleation sites to anchor metallic nanoparticles strongly. Strong synergy between N-doped graphene and $ZnCo_2O_4$ is observed as a high-performance anode electrode material for much higher capacity levels and more durable electrochemical stability in lithium ion batteries. The mesoporous nanoarchitecture electrode shows enhanced reversible performance in cyclic anode tests, maintaining a specific energy capacity of 998 mAh $g^{-1}$ after 30 cycles at current density of 100 mA $g^{-1}$.


## 1. Introduction

Lithium ion batteries (LIBs) are among the most broadly used electronic gadgets of this century [1]. Due to their high energy density, LIBs are actively utilized as major power sources for portable electronic devices such as mobile phones, notebook computers, tablet computers, digital cameras, flashlights, and laptop computers. Thus far, single or binary transition-metal oxides have been strongly considered as anode electrode materials for LIBs given their high storage capacities for the past few decades due to their versatile physical and chemical properties and their extraordinary reversible capacities [2–4]. Nano-sized Cu, Fe, Ni, and Co oxides have demonstrated high electrochemical capacities and superior cyclic stability [5]. Several metal oxides along with a few carbon-based materials also exhibited superior anodic performances for LIBs [6–9]. However, ternary-metal oxides have not been explored significantly for high-performance anode electrode materials in LIBs as compared to binary metal oxides.

In recent years, mixed transition-metal oxides (MTMOs) with stoichiometric ratios or non-stoichiometric ratios have been considered to be very promising candidates for different energy-related applications. In general, a sophisticated combination of two low-cost transition metals leads to the formation of MTMOs. These MTMOs mainly function as single-phase ternary-metal oxides rather than as a simple mixture of two binary-metal oxides. Owing to the presence of multiple valences of the cations, high electrical properties, and the synergetic effect of these characteristics, these new classes of transition-metal oxides are capable of providing desirable electrochemical behavior which is primarily useful for LIB applications. For the last several years, various MTMOs such as $NiCo_2O_4$, $FeCo_2O_4$, $MgCo_2O_4$, $ZnCo_2O_4$, $MnCo_2O_4$, $CoMn_2O_4$, $ZnMn_2O_4$, and $ZnFe_2O_4$ have been investigated for LIB applications [10–18].

Among these MTMOs, $ZnCo_2O_4$ has been most widely studied for LIB applications in recent years. This metal oxide has a spinel structure in which bivalent Zn-ions occupy the tetrahedral sites and trivalent Co-ions occupy the octahedral sites. This particular alignment of metals allows $ZnCo_2O_4$ to undergo a conversion reaction between the metal species and Li while also participating in the reaction between Zn and Li, therefore enhancing the lithium

* Corresponding author.
*E-mail address:* ikoh@kaist.ac.kr (I.-K. Oh).
[1] These authors contributed equally to this work.

http://dx.doi.org/10.1016/j.carbon.2015.07.024
0008-6223/

storage capacity. Although various nanoarchitectures of $ZnCo_2O_4$ such as nanoparticles, porous nanoflakes, and nanowires have been investigated for LIB applications, hybrid materials based on MTMOs and carbonaceous materials have not been explored widely thus far. Liu et al. reported the fabrication of an anode material for LIBs based on hierarchical three-dimensional $ZnCo_2O_4$ nanowire arrays and carbon cloth [19]. The remaining main issue associated with hybrid electrodes is to create a strong bond between MTMOs and carbonaceous materials. Strong bond between MTMOs and carbonaceous materials closely contributes to high cyclic stability in electrochemical tests. The synergistic interaction between the MTMOs and carbon base materials plays an important role to enhance the electrochemical performances of the composite.

Among the various forms of carbon allotropes, graphene, defined as a single-carbon-atom-thick $sp^2$ hybridized honeycomb lattice, has demonstrated tremendous application potentials in various energy related fields including LIBs. Graphene and reduced graphene oxide (rGO) have been considered as an efficient anode material for LIBs due to their high surface area, excellent electrical properties, and extraordinary mechanical flexibility. However, current studies have closely examined the surface modification of graphene. Heteroatom-doped graphene has shown superior Li storage capabilities. Among the various hetero-atoms, nitrogen (N) is the superior dopant for graphene, because the atomic sizes of C and N are similar. Further, N-doping enhances the Li-adsorption energies due to the higher electronegativity of N as compared to C, and due to the hybridization between the N lone pair and the $\pi$ system of graphene [20–22]. Reddy et al. demonstrated the direct growth of N-doped graphene films on Cu through a CVD process, demonstrating nearly double the reversible discharge capacity as compared to pristine graphene [23]. Wu et al. reported the synthesis of N-doped graphene through a heat treatment of graphene in a $NH_3$ atmosphere, showing reversible capacities of 1043 mAh $g^{-1}$ with 83.6% reversible capacity retention after 30 cycles [24]. Wang et al. prepared N-doped graphene nanosheets through a heat treatment of graphene oxide in a $NH_3$ atmosphere with a 2 at.% nitrogen content, exhibiting a high reversible capacity of 900 mAh $g^{-1}$ at a current density of 42 mA $g^{-1}$ and reversible capacity of 250 mAh $g^{-1}$ at a current density of 2.1 A $g^{-1}$ [25]. Although N-doped graphene has been extensively investigated for LIB applications, nanohybrids based on metal oxide and N-doped graphene have not been explored as much. Li et al. reported the in-situ growth of anatase $TiO_2$ nanoparticles on N-doped rGO which exhibited average reversible capacities of 226 mAh $g^{-1}$ at a current rate of 0.2 C [26]. Jiang et al. demonstrated a three-dimensional foam architecture of ultrafine $TiO_2$ nanoparticles embedded in N-doped graphene networks through a combined process hydrothermal self-assembly and freeze drying. The electrode material showed a reversible capacity of 165 mAh $g^{-1}$ after 200 cycles at a 1 C rate and a reversible capacity of 143 mAh $g^{-1}$ after 200 cycles at a 5 C rate [27]. In a recent study, Yang et al. demonstrated the hydrothermal synthesis of a $MnO_2$/N-doped graphene composite using polypyrrole as the N source, exhibiting a reversible capacity of 647.5 mAh $g^{-1}$ at a current density of 100 mA $g^{-1}$ [28].

However, no reports are available on a defect-engineered synthetic method to produce a well-dispersed mesoporous ternary nanoarchitecture with strong bonding between MTMO and graphene. In this work, we report a novel mesoporous nanoarchitecture of $ZnCo_2O_4$/N-doped graphene that is synthesized through a defect-engineered hydrothermal and thermal annealing process and their potential as anode materials for LIB applications. The novel hetero-nanostructure with a high surface area enabled N-doped graphene/$ZnCo_2O_4$ to exhibit outstanding electrochemical performance. To the best of our knowledge, this is the first report on the LIB application of nanohybrids based on MTMO and N-doped graphene, as well as the first report of a structural and property analysis of nanohybrids based on $ZnCo_2O_4$ and graphene/N-doped graphene.

## 2. Experimental

### 2.1. Preparation of self-assembled materials

#### 2.1.1. Materials

$Zn(NO_3)_2$hexahydrates, $Co(NO_3)_2$hexahydrates and urea were supplied by Sigma Aldrich. Ethanol and hydrazine monohydrate were purchased from Daejung Chemicals and Metals Co. Ltd. All chemicals were utilized as received, without further distillation. For the synthesis of graphene oxide, graphite powder was purchased from Samjung C&G (99.95%). Other chemicals, in this case $H_2SO_4$, $H_3PO_4$, $KMnO_4$, $H_2O_2$, and HCl, were obtained from Sigma Aldrich.

#### 2.1.2. Preparation of $ZnCo_2O_4$ (ZCO)

In a typical process, initially 1 mmol of $Zn(NO_3)_2$, $6H_2O$ and 2 mmol of $Co(NO_3)_2$, $6H_2O$ were dispersed in 40 ml of DI water. Then, 4 mmol of $Co(NH_2)_2$ and 10 ml of ethanol were slowly added to the solution. Subsequently, the entire solution was vigorously stirred for 1 h. After stirring, the solution was transferred to a 100-ml Teflon-lined autoclave and heated at 120 °C for 6 h. After the autoclave cooled to room temperature, the product was collected, washed with water and ethanol through centrifugation and then dried at 60 °C. Finally, the pink-colored product was thermally treated at 400 °C for 2 h. After the thermal treatment, the pink power became black ZCO.

#### 2.1.3. Preparation of rGO/$ZnCo_2O_4$ (GZCO)

A similar process was adopted for the preparation of GZCO. In this process, instead of DI water, transition-metal oxide precursors [$Zn(NO_3)_2$, $6H_2O$ and $Co(NO_3)_2$, $6H_2O$] were dispersed in a GO solution (5 mg/ml). Finally the obtained black-colored product, through a hydrothermal reaction, was thermally treated at 400 °C for 2 h in an Ar atmosphere to obtain the nanohybrids.

#### 2.1.4. Preparation of N-doped graphene/$ZnCo_2O_4$ (NGZCO)

Hydrazine monohydrate was used as a N-doping precursor. First, transition-metal oxide precursors were dispersed in 5 mg/ml GO solution through sonication. Subsequently, 1 mmol of hydrazine monohydrate was added to the solution, followed by further sonication. After the hydrothermal reaction, the obtained black-colored powder was thermally treated at 400 °C for 2 h in a $N_2$ atmosphere in order to obtain NGZCO.

### 2.2. Characterization

The physical characterization of the unique mesoporous $ZnCo_2O_4$/N-doped graphene nanoarchitecture was examined using X-ray diffractometry (XRD, D/MAX-2500, Japan), field-emission scanning electron microscopy (FESEM, Magellan-400, Nova230, Japan), transmission electron microscopy (FETEM, Tecnai F20, U.S.A.), high-resolution dispersive Raman spectroscopy (LabRAM HR UV/Vis/NIR, France), Fourier-transform infrared spectroscopy (FT-IR, 4100 Jasco, Japan), multipurpose X-ray photoelectron spectroscopy (XPS, Sigma Probe, U.K.), Brunauer Emmett Teller (BET, Tristar ll 3020 V1.03, Micromeritics, U.S.A.) surface area characterization and a thermogravimetric analysis (TGA, 92-18, Setaram, France). The electrochemistry of the electrode materials was studied using CR2032 coin cells. The ratio of active material, conducting carbon (Ketzen black), and binder (Teflonized acetylene black) was

70:15:15 by weight. The components were mixed thoroughly using ethanol and the resulting thin film was pressed on a stainless steel disk. The electrode disks were 1.6 cm in diameter with an active material loading of 2.5 mg $cm^{-2}$. The electrodes were dried at 160 °C for 4 h before the cell assembly process. Metallic Li foil was used as a counter electrode. A 1 M solution of $LiPF_6$ in Ethylene Carbonate/Dimethyl Carbonate (1:1 v/v) was used as the electrolyte. The electrodes were separated by a microporous poly propylene separator (Celgard, USA). Cyclic voltammetry and electrochemical impedance spectroscopy data were obtained using an electrochemical work station (SP-150, Bio-logic, France). The frequency range was varied from 100 kHz to 100 mHz for electrochemical impedance spectroscopy studies under an applied voltage of 10 mV. The coin cells were cycled galvanostatically between 0 and 3 V with a battery tester (WBCS 3000, Won-A-Tech, Korea).

## 3. Results and discussion

### 3.1. Morphology and structural analysis

A facile two-step hydrothermal reaction followed by thermal annealing was utilized for the synthesis of ZCO, GZCO, and NGZCO. Based on few previous studies and on the morphological and as well as structural features, we proposed the probable formation mechanism of these three different types of nanohybrids, as schematically illustrated in Fig. 1. For ZCO, upon the first sonication, the interweaving of $Zn^{2+}$ and $Co^{3+}$ cations with ethanol molecules form nanoscale clusters (first-step). Under a hydrothermal reaction, nanoclusters started to nucleate and forms regular granules (second-step). In order to reduce their surface energy and due to their tendency to aggregate randomly, these granules started to form nanosheets (third-step) and sustained this action to form a flower-like porous network (forth-step) [12,29]. Further, thermal annealing led to the formation of a flower-like mesoporous architecture (fifth-step). For graphene-based nanohybrids, regular granules of the metal cations arranged themselves on the rGO sheets after nucleation and aggregation under a hydrothermal process. The rGO skeletons were acted as superior templates for the growth and formation of nanosheets of a mixed transition-metal oxide. However, due to the weak bonding between the rGO and $ZnCo_2O_4$, a few rGO sheets remained uncoated. For the mesoporous $ZnCo_2O_4$/N-doped graphene (NGZCO), the N-doping precursor was thermally decomposed and nitrogen atoms were incorporated into the graphene network under a hydrothermal process. Atomic-scale defects such as nitrogen-doped sites and oxygen-functional groups in the chemically modified graphene oxide enhanced the bonding between rGO and $ZnCo_2O_4$. With regard to this point, the hydrothermal process played a crucial role both in the nitrogen doping and the growth of the nanosheets. Hence, all rGO skeletons were uniformly covered by the nanosheets after nucleation and aggregation under the hydrothermal condition. Furthermore, the thermal annealing process removed residual oxygen functional groups from the rGO sheets and led to the formation of a flower-like porous morphology with closely packed sheets and a few undisturbed rGO sheets. Finally, a well-defined flower-like morphology was observed for NGZCO.

Structural and morphological analyses of ZCO, GZCO and NGZCO were conducted with SEM and HRTEM imagery. The SEM images of ZCO show the flower-like morphology of the $ZnCo_2O_4$ spheres as shown in Fig. 2(a) and (b). The $ZnCo_2O_4$ spheres are composed of closely packed sheets. A similar type of morphology was observed by Hu et al. [12]. This flower-like porous microstructure is responsible for the high surface area of ZCO. However, as observed in the SEM image of GZCO, the flower-like $ZnCo_2O_4$ spheres remain intact in the presence of graphene, although a few graphene sheets remain uncoated as shown in Fig. 2(c). A SEM image at a high magnification reveals the porous nature of the GZCO in Fig. 2(d). The NGZCO shows a completely different type of morphology. Closely packed nanoparticles are anchored onto the surfaces of the N-doped rGO sheets in Fig. 2(e), while Fig. 2(f) indicates the porous nature of NGZCO. The high- and low-magnification SEM images illustrate the interconnecting network structure and micrometer-sized rough surface morphology of the NGZCO. This type of porous interconnecting network-like structure is essential for the reduction of the mechanical stress caused by the volumetric changes which arise during charging–discharging cycling [28].

The HRTEM analysis delivers further structural information about the nanohybrids. As observed in Fig. 3(c), the edges of the $ZnCo_2O_4$ microspheres are composed of nanoparticles. The lattice fringes indicate the presence of random pores in the ZCO. The spacing between the lattice plans is found to be 0.24 nm, indicating the (3 1 1) plane of $ZnCo_2O_4$, as shown in Fig. 3(d). The elemental mapping confirms the presence of Zn, Co, and O species in the ZCO. HRTEM images of GZCO show a wormhole-like porous morphology. However, a few uncoated graphene layers are also observed in Fig. 3(e), which may be due to the weak interfacial bonding between the rGO and the ternary transition-metal oxide particles. However, the high-resolution image of GZCO shown in Fig. 3(f) indicates the (3 1 1) plane of $ZnCo_2O_4$, while the elemental mapping confirms the presence of C, Zn, Co, and O species. The typical TEM micrograph of NGZCO shows the novel wormhole-like porous system. A uniform distribution of the ternary-metal oxide particles on N-doped rGO surfaces is clearly shown in Fig. 3(a). The N-doped rGO framework acted as a superior template for the proper dispersion of the metal-oxide particles as the doping of nitrogen reduces the particle size and hence enhances the dispersion. Further, N-doping creates numerous defects on the rGO sheets and thus enhances the reactive nucleation sites. As a result, the interactions between the $ZnCo_2O_4$ and N-doped rGO sheets are improved. Similar to other nanohybrids, NGZCO also shows a fringe spacing of 0.24 nm, indicative of the (3 1 1) plane of $ZnCo_2O_4$, as shown in Fig. 3(b). The elemental mapping confirms the presence of C, N, Zn, Co, and O species in NGZCO. Close contact between N-doped rGO sheets and $ZnCo_2O_4$ particles can enhance the electrochemical performance by improving the rate of electron transport during cyclic charging–discharging.

A BET $N_2$ adsorption–desorption analysis was carried out to determine the specific surface area and average pore-size distribution of the $ZnCo_2O_4$-and $ZnCo_2O_4$-based nanohybrids at 77.3 K. The BET $N_2$ adsorption–desorption analysis data are summarized in Table 1, and the corresponding $N_2$ adsorption–desorption isotherms and pore-size distribution curves are shown in Fig. 4. In this study, the surface area was chosen as the prime parameter to optimize the concentration of graphene oxide for the preparation of the NGZCO. ZCO exhibits a surface area of 34.4 $m^2/g$. The surface area of an electrode material has been observed to increase drastically with an addition of rGO. Among all of the rGO-based nanohybrids, $ZnCo_2O_4$/rGO (GZCO, 5 mg/ml GO conc.) exhibits the highest surface area of 69.5 $m^2/g$, which was found to be double the surface area of ZCO. This significant increment of the surface area is due to the high surface area of rGO. Strong bonding between rGO and the mixed transition-metal oxide enhances the surface area of GZCO. However, with an increase of the concentration of graphene oxide, the surface area decreases, as listed in Table S1. As the nanohybrids exhibits the highest surface area at 5 mg/ml GO concentration, this particular concentration was utilized for the doping process (NGZCO). After nitrogen doping, the surface area increases (73.6 $m^2/g$) due to the formation of a large number of surface defects upon the incorporation of N atoms into the

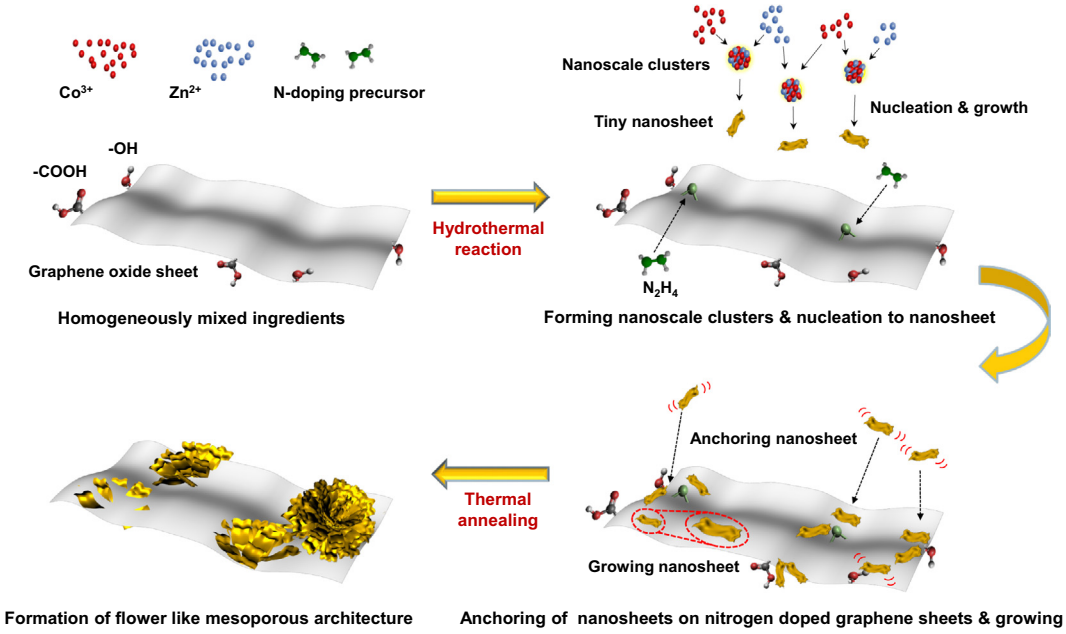


**Fig. 1.** Schematics of the preparation of NGZCO.

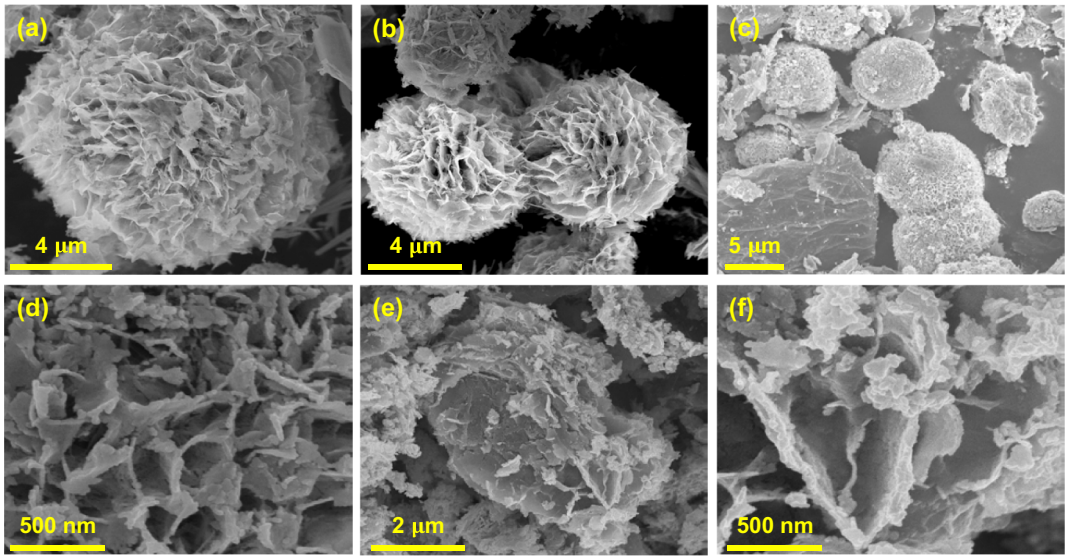


**Fig. 2.** SEM images of (a, b) ZCO and (c, d) GZCO under low and high magnification, and (e, f) NGZCO under low and high magnification.

graphene layers. The average pore size for all of the electrode materials was obtained from the desorption data and calculated from the isotherm using the BJH model. The average pore size decreases with an addition of rGO and N-doped rGO. With the addition of rGO and with the doping process, the specific surface area increases and the average pore size decreases, whereas the average pore volume remains nearly identical. Hence, the number of pores increases, which is coincident with the HRTEM analysis. All of the sorption isotherms are type IV isotherms, indicative of the mesoporous nature. GZCO exhibits a distinguished H2-type hysteresis loop, whereas ZCO and NGZCO show distinct H4-type hysteresis loops. This porous nature helps the nanohybrids to compensate for the large volume change of the anodes during the repeated $Li^+$ insertion-extraction process [29–31].

A XPS analysis was conducted to understand the chemical nature and elemental valence of the nanohybrids. The XPS spectra of ZCO, GZCO and NGZCO are shown in Figs. S2, S3, and Fig. 5, respectively. The survey scan spectrum of each nanohybrid confirms the presence of Zn, Co, and O species in ZCO; Zn, Co, O, and C in GZCO; and Zn, Co, O, C, and N species in NGZCO. The high-resolution Zn 2p spectrum shows two strong peaks at 1045.7 and 1022.6 eV, which can be assigned respectively to Zn $2p_{1/2}$ and Zn $2p_{3/2}$, confirming the Zn(II) oxidation state of $ZnCo_2O_4$, as shown in Fig. S2(b). Further, the high-resolution spectrum of Co 2p in Fig. S2(c) displays two strong peaks at 796.6 and 781.1 eV, which may be attributed to Co $2p_{1/2}$ and Co $2p_{3/2}$, respectively, indicating the Co (III) oxidation state [32,33]. The peaks at 530.5 and 532.1 eV in the O 1s spectrum shown in Fig. S2(d) confirm the presence of oxygen species in ZCO. The XPS spectra of GZCO show the characteristic peaks of Zn $2p_{1/2}$, Zn $2p_{3/2}$, Co $2p_{1/2}$, Co $2p_{3/2}$ and O 1s, but, the peaks positions are slightly shifted due to the bonding between the rGO and $ZnCo_2O_4$, as listed in Table S2. Additionally, the C 1s

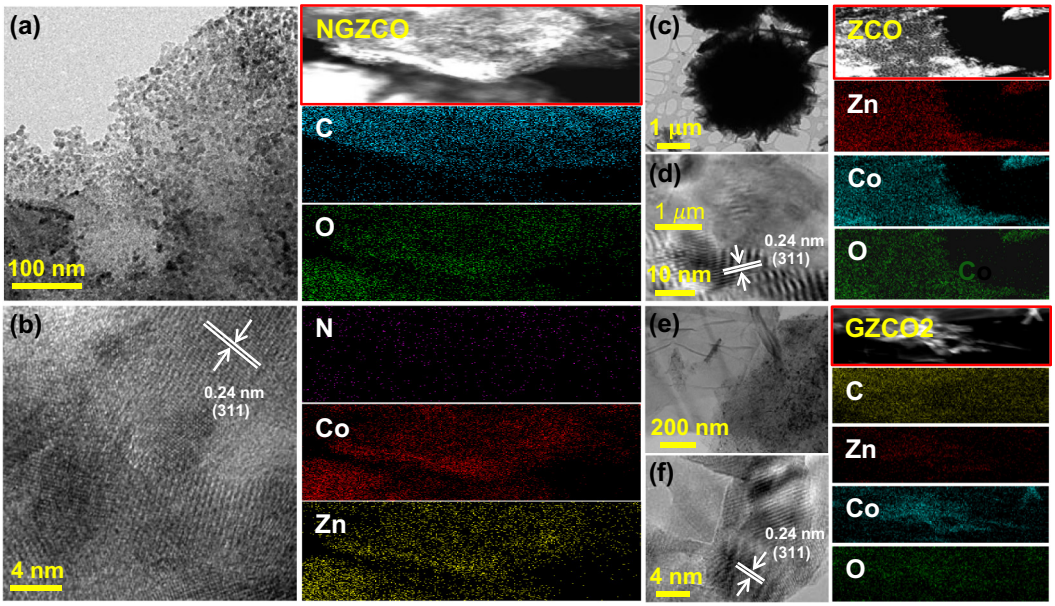


**Fig. 3.** HRTEM images and corresponding elemental mapping of (a, b) NGZCO, (c, d) ZCO, and (e, f) GZCO.

**Table 1**
Composition of the BET surface area, pore volume and average pore size of ZCO, GZCO and NGZCO.

| Sample name | Surface area ($m^2$/g) | Pore Volume ($cm^3$/g) | Average Pore Size (nm) |
|---|---|---|---|
| ZCO | 34.4 | 0.3009 | 37 |
| GZCO | 69.5 | 0.3029 | 14 |
| NGZCO | 73.6 | 0.2911 | 15.9 |

spectrum in Fig. S3 shows a broad peak at 284.6 eV, which can be attributed to the $sp^2$ C–C bond. Most importantly, the XPS spectra of NGZCO indicate a significant signal of the N species, confirming the N-doping of rGO in the presence of $ZnCo_2O_4$. The N 1s spectrum of NGZCO shows sharp peaks at 401.7 and 400.2 eV, which can be assigned to graphitic N and pyrrolic N, respectively. The pyrrolic N component is dominant. However, the weak peak at 398.3 eV indicates the presence of pyridinic N as well in Fig. 5(c). The N content in NGZCO was found to be 2.38 wt.%, which is higher than a previously reported value [28]. The high-resolution C 1s shows four peaks at 284.6 eV (C–C), 285.7 eV (C═N), 286.5 eV (C–OH, C–N) and 288.7 eV (C═O). It is important to note that the presence of C═N and C–N bonds indicate N doping in Fig. 5(d). The XPS analysis confirms the N doping of rGO in NGZCO. This analysis also confirms the presence of strong synergistic effects between the N-doped rGO and the MTMO, which is essential to achieve high cyclic stability. For a further confirmation, a FTIR analysis of the nanohybrids was performed.

Fig. 6(a) represents the FTIR spectra of all of the nanohybrids. The FTIR spectrum of ZCO shows two characteristic absorption bands at 587 and 669 $cm^{-1}$ due to the M–O stretching vibration mode for octahedrally and tetrahedrally coordinated metal ions [34–36]. The shape peak at 3452 $cm^{-1}$ is attributed to the hydroxyl group of the adsorbed water. For GZCO, the characteristic peaks of $ZnCo_2O_4$ are red-shifted by 10 and 16 $cm^{-1}$. Moreover, the FTIR spectrum of GZCO shows the presence of C═O carbonyl stretching (1700 $cm^{-1}$), C–O alkoxy stretching (1129 $cm^{-1}$), C–O epoxy stretching (1226 $cm^{-1}$) and broad peak at approximately 3447 $cm^{-1}$ due to the presence of an adsorbed water moiety. However, the sharp peak at 1568 $cm^{-1}$ can be assigned to the skeletal vibration of the graphene sheets [32]. The FTIR spectrum of NGZCO shows all of the characteristic peaks of $ZnCo_2O_4$ and rGO with slightly shifted positions. Most importantly, as compared to ZCO and GZCO, the characteristic peaks of $ZnCo_2O_4$ become more sharpened for NGZCO, which indicates the strong bonding between the N-doped rGO and $ZnCo_2O_4$.

A Raman spectral analysis was undertaken to investigate the spectral features of the nanohybrids as well as the doping effect of rGO. Fig. 6(b) compares the Raman spectra of ZCO, GZCO and NGZCO. For ZCO, two Raman active peaks are observed at 556.5 and 650.2 $cm^{-1}$, corresponding to the characteristic $F_{2g}$ and $A_{1g}$ modes of $ZnCo_2O_4$ [37]. The $A_{1g}$ mode represents the disorderness caused by the substitution of Zn at the Co octahedral sites in the spinel lattices, and $F_{2g}$ represents the spinel phases of $ZnCo_2O_4$ [38].

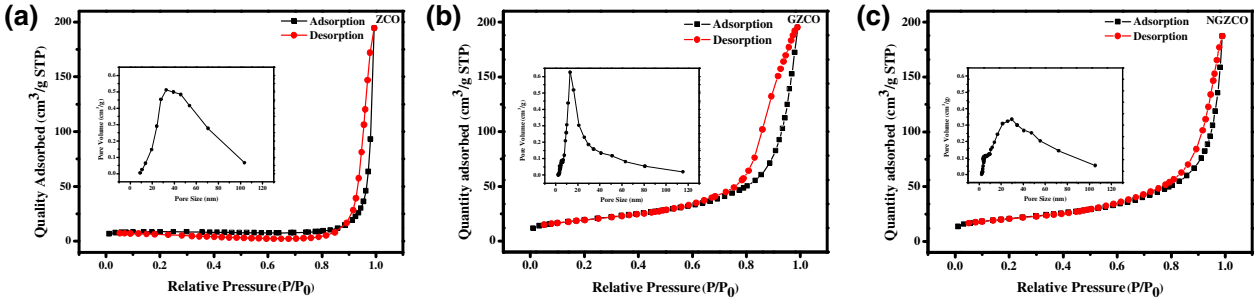


**Fig. 4.** Nitrogen adsorption and desorption isotherms and corresponding pore-size distribution curves (insets) of NGZCO, GZCO and ZCO.

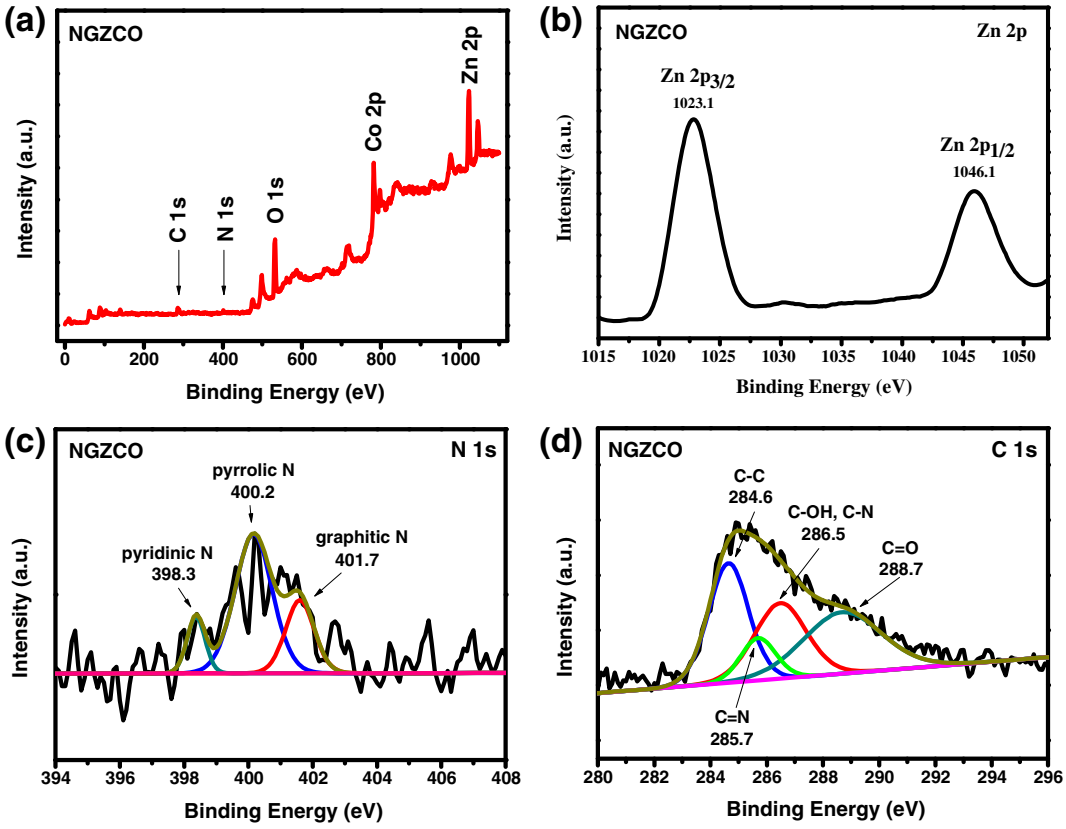


**Fig. 5.** XPS analysis: (a) XPS survey spectrum and the C 1s, N 1s, O 1s, Co 2p, and Zn 2p spectra of NGZCO; and (b) Zn 2p, (c) N 1s, and (d) C 1s peaks of NGZCO.

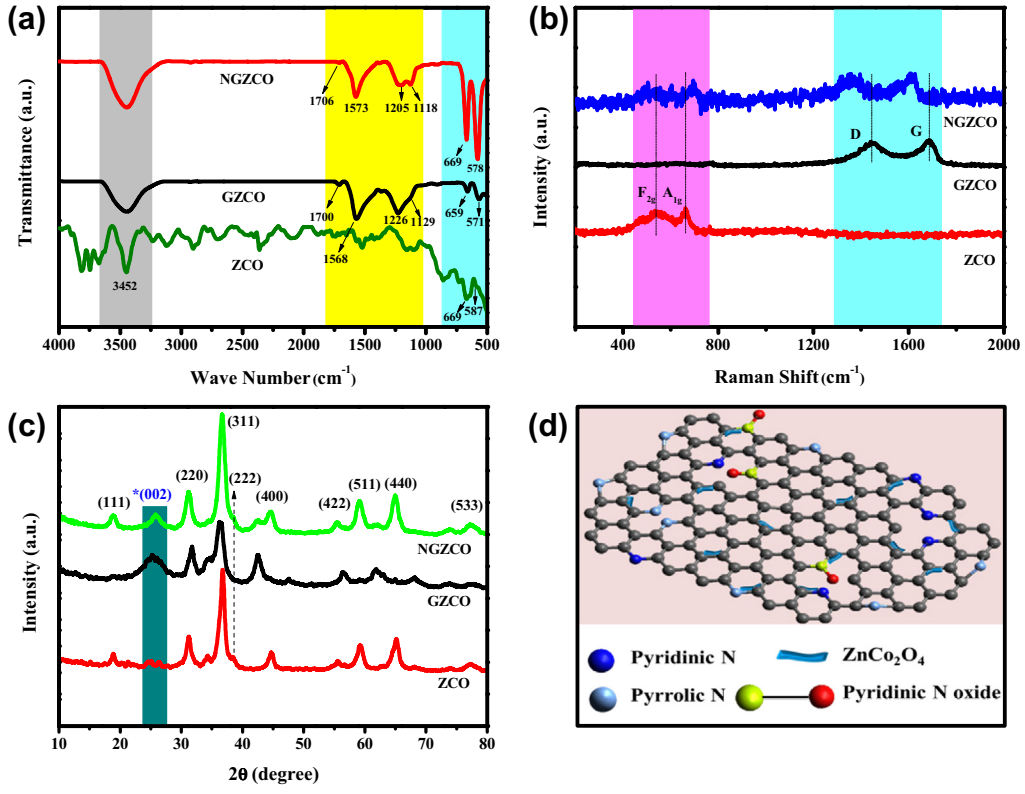


**Fig. 6.** Chemical and structural characterizations; (a) FTIR, (b) Raman spectra, and (c) XRD spectra of ZCO, GZCO, and NGZCO; and (d) schematic presentation of NGZCO, showing different N environments.

Interestingly, the types of characteristic peaks of ZCO are not observed in the Raman spectra of GZCO. This anomalous phenomenon may be caused by the weak interaction between the ternary-metal oxide and the rGO. In general, rGO shows a characteristic D band (~1350 $cm^{-1}$), initiated by the formation of defects caused by the breathing mode of $A_{1g}$ symmetry and the G band (~1580 $cm^{-1}$); this is associated with the mode of $E_{2g}$ symmetry and related to the degree of graphitization [39]. However, for GZCO, the characteristic D and G bands are blue-shifted to 1445.5 and 1687 $cm^{-1}$, respectively. The upshifting of the D band may be caused by the enhancement of electron–photon coupling [40]. The shifting of the band position of GZCO confirms the presence of rGO and metal oxide, instead of only rGO. The $I_D/I_G$ ratio of 0.996 represents the formation of a subsequent $sp^3$ domain. In contrast, the characteristic peaks of the D band and G band of rGO as well as the $A_{1g}$ and $E_{2g}$ modes of $ZnCo_2O_4$ are clearly visible in the Raman spectrum of NGZCO, but in slightly shifted positions. As compared to GZCO, the D band and the G band are red-shifted to 1359 and 1594.5 $cm^{-1}$, respectively. This phenomenon can be explained by the empirical relationship between the Fermi energy and the Raman Peak position. The N dopants in NGZCO move up the Fermi level of rGO and thus cause the downshifting of the D and G bands [41]. The $I_D/I_G$ ratio of NGZCO (1.006) was found to be higher than that of GZCO, which suggests the formation of a large number of defects caused by N doping and a proper reduction of GO to rGO in the presence of ternary-metal oxide. Moreover, the characteristic $A_{1g}$ and $E_{2g}$ modes of $ZnCo_2O_4$ are also shifted for NGZCO due to the superior interaction between $ZnCo_2O_4$ and N-doped rGO.

Fig. 6(c) depicts the XRD patterns of ZCO, GZCO and NGZCO. In the XRD pattern of ZCO, the peaks at $2\theta = 18.9°$, 31.26°, 36.78°, 38.41°, 44.74°, 55.57°, 59.24°, 65.17° and 77.32° are correspondingly attributed to the reflections of the (111), (220), (311), (222), (400), (422), (511), (440) and (533) planes of $ZnCo_2O_4$. The diffraction profile of ZCO shows significant characteristics of cubic $ZnCo_2O_4$ with a spinel structure (JCPDS Card No. 23-1390). No other additional peaks are observed, which indicates the absence of any other metal oxides or impurities. However, the XRD pattern of GZCO shows an additional broad peak at 25.34°, indicating the (002) plane of graphitic carbon [42]. The peak intensities of the characteristic peaks of $ZnCo_2O_4$ were decreased for GZCO. This can be explained by the weak interaction between rGO and $ZnCo_2O_4$. The XRD pattern of NGZCO shows all of the characteristic peaks of $ZnCo_2O_4$. Further, the broad peak at around 25.74° can be attributed to the disordered rGO layers. As compared to GZCO, the peak intensities of all of the characteristic peaks are enhanced, indicating strong bonding and superior compatibility between the N-doped rGO and $ZnCo_2O_4$. This observation is in good agreement with the results of the morphological analysis of the nanohybrids. Most importantly, the characteristic peak at 10.4° for GO is entirely absent in the XRD patterns of GZCO and NGZCO. Based on the XPS and FTIR analyses results, the probable structure of NGZCO has been explored, as schematically shown in Fig. 5(d), which represents different types of N environments of N-doped rGO in the presence of $ZnCo_2O_4$.

### 3.2. Li-ion batteries performance

Fig.7(a) shows the first discharge–charge curves of ZCO, GZCO and NGZCO as evaluated under galvanostatic conditions at a current density of 0.1 A $g^{-1}$ against metallic lithium. All of the samples exhibit excellent electrochemical performance with a first discharge capacity amounting to 1897, 1884 and 1842 mAh $g^{-1}$, respectively, which is correlated to a consumption of ~17 mol equivalents of lithium per mole of $ZnCo_2O_4$. The initial capacity values expressed here are higher than in other reports in the literature [43,44] and thus complement the morphological features and higher surface areas obtained, especially for the NGZCO sample. The characteristic discharge curves show have a sudden drop from the open-circuit potential until 1.3 V, representing the starting point of the conversion reaction and the destruction of the structure of $ZnCo_2O_4$ to form corresponding metals without the Li intercalation reaction [44]. A flat potential plateau was observed as the voltage fell from 1.3 to 0.7 V which corresponds to alloy formation between Lithium and Zinc. A further reduction in the voltage led to a continuously decreasing voltage profile, representing the formation of the SEI layer. Metallic Zinc and Cobalt formed during the initial discharge and were then converted to the representative oxides of ZnO, CoO and $Co_3O_4$ during the subsequent charging cycle. Therefore, the initial discharge reaction is irreversible and the oxides formed during the initial charging cycle remain active during further cycling and are responsible for the reversibility of the representative negative electrode material. The reversible Li storage in $ZnCo_2O_4$ is based on the conversion reaction mechanism. It undergoes the following electrochemical reactions:

$$ZnCo_2O_4 + 8Li + 8e^- \rightarrow Zn + 2Co + 4Li_2O$$

$$Zn + Li^+ + e^- \leftrightarrow LiZn, (LiZn \rightarrow Li_2Zn_3 \rightarrow LiZn_2 \rightarrow Li_2Zn_5 \rightarrow LiZn_4)$$

$$Zn + Li_2O \leftrightarrow ZnO + 2Li^+ + 2e^-$$

$$2Co + 2Li_2O \leftrightarrow 2CoO + 4Li^+ + 4e^-$$

$$2CoO + 2/3Li_2O \leftrightarrow 2/3Co_3O_4 + 4/3Li^+ + 4/3e^-$$

During the first charging cycle, up to 3.0 V, all three samples regained their charge capacity equivalent to ~50% of the Coulombic efficiency. The charge curves showed two distinct plateaus at 1.7 and 2.1 V, which represents the formation of oxides of Zn and Co. The voltage profiles of the discharge–charge reaction match the electrochemical reactions well. The distinct feature of NGZCO compared to ZCO and GZCO is the decrease in the voltage polarization, which is considered to be the difference in the plateau voltage between the charge and discharge curves; hence, good cycle ability is presumed.

The cycle performance curves of ZCO, GZCO and NGZCO are presented in Fig. 7(b). The bare ZCO sample retained a higher discharge capacity compared to GZCO and NGZCO for the initial 10 cycles, with a second-cycle discharge capacity of 1128 mAh $g^{-1}$ and capacity retention (from 2 to 10 cycles) of 91%; however, the discharge capacity decreased to 470 mAh $g^{-1}$ after 30 cycles and the cycle efficiency was reduced to 42%. On the other hand, the presence of graphene improved the cycle efficiency of GZCO to 81% after 30 cycles due to the enhanced connectivity between the particles and the improved electronic conductivity. For the N-doped graphene composite, NGZCO, the second cycle discharge capacity was 1045 mAh $g^{-1}$ and the capacity retained after 30 cycles was 998 mAh $g^{-1}$ at 0.1 A $g^{-1}$ with capacity retention of 95%. The capacity retention of NGZCO is higher than those of ZCO and GZCO due to the presence of uniformly distributed ZCO particles over the N-doped graphene, the formation of a highly conducting network due to the complete reduction of graphene, the ability to accommodate volume changes effectively due to high porosity, and the presence of defects in the N-doped graphene which improves the reactivity of the meal oxide during the discharge–charge reactions. Another important aspect of the composite materials is that the Coulombic efficiency was regained to nearly 97% and 99% for GZCO and NGZCO, respectively, after the initial cycle, while the ZCO sample had a slow recovery of the Coulombic efficiency 91% within a few cycles and maintained this level up to 30 cycles, which explains the continuous decreasing cycle life for ZCO. The lower Coulombic efficiency implies higher

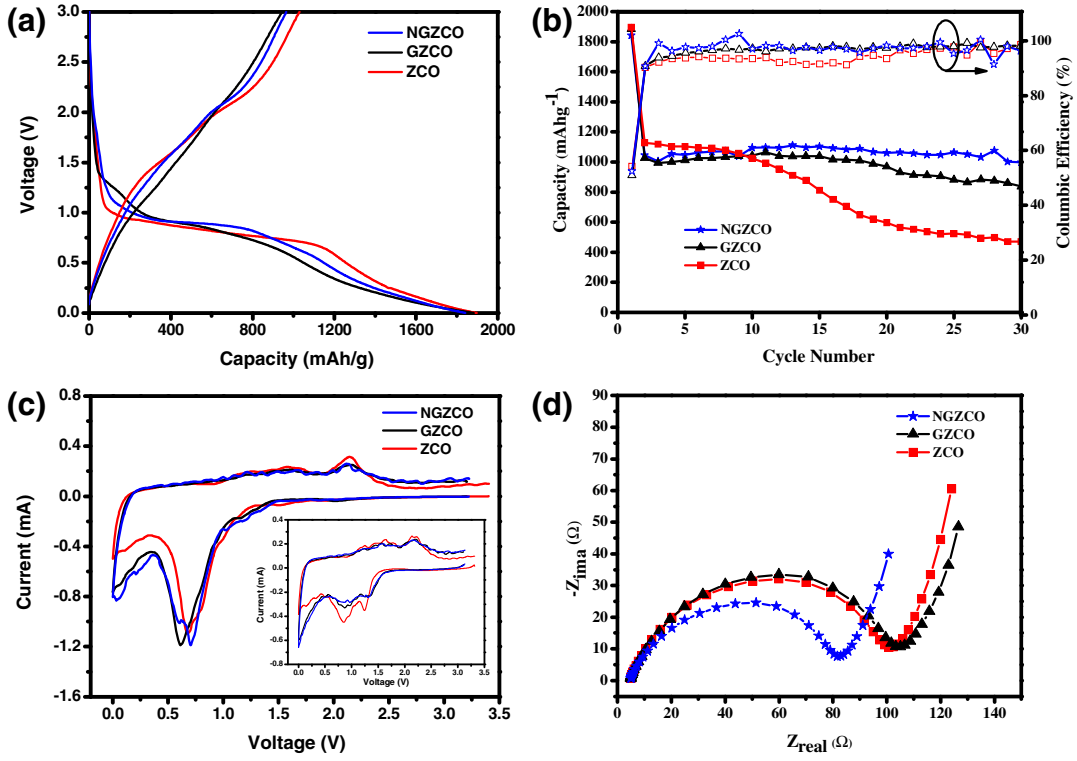


**Fig. 7.** Electrochemical data of the ZCO, GZCO and NGZCO samples: (a) galvanostatic first discharge–charge curves at 0.1 A $g^{-1}$. (b) Cycle life and Coulombic efficiency curves at 0.1 A $g^{-1}$. The closed symbols represent the capacity and the open symbol denotes the Coulombic efficiency. (c) Cyclic voltammograms of the samples at 50 μV $s^{-1}$ vs metallic lithium. The data representing the second cycle is given in the inset. (d) Electrochemical impedance spectroscopy curves measured between 100 kHz and 100 mHz.

consumption of the electrolyte and lithium during the decomposition process, which in turn affects the cycle life [45]. Thus, the cycle life data obtained for the ZCO, GZCO and NGZCO samples are substantiated.

In order to corroborate the results obtained from the discharge–charge studies, cyclic voltammograms are recorded between 0 and 3 V at a 50 μV $s^{-1}$ scan rate. These results are shown in Fig. 7(c). During the initial reduction cycle, an uninterrupted profile was observed until the voltage reached 1.5 V; a further reduction leads to the destruction of $ZnCo_2O_4$ and the subsequent formation of a sharp peak at 0.7 V corresponding to metal formation and the alloying of Li and Zn. A further reduction leads to the formation of a SEI layer, which is marked by the peak near 0 V. During the subsequent oxidation process, two notable peaks at 1.7 and 2.1 V are observed; theses can be attributed to the oxidation of metallic Zn and Co. The conversion reaction follows a different mechanism from the second cycle onward, as clearly observed from the shift in the reduction peaks to 1.3 and 0.8 V, while the oxidation peaks does not change. The cyclic voltammetry results for ZCO, GZCO and NGZCO followed a similar pattern for all of the samples. In addition, the data was in good agreement with the electrochemical reactions and the corresponding discharge–charge curves obtained through galvanostatic cycling studies, in accord with the findings in other reports [13,35,44]. The effect of the internal charge transfer resistance of the as-prepared half cells will be helpful to those assessing the cause of the improved performance levels of NGZCO as compared to the levels of ZCO and GZCO. Electrochemical impedance spectroscopy was conducted to determine the resistance of the as-prepared cells. The impedance plots consists of a semicircle that intercepts the real axis in a high-frequency region, representing the solution resistance due to the electrolyte, while the other end of the semicircle meets the real axis at a medium-to low-frequency region which corresponds to the total resistance of the cell. The difference between the total and solution resistance gives the charge transfer resistance encountered by the electrode material. The sloping line in the low-frequency region is related to the diffusion of lithium ions in the electrode. A calculated charge transfer resistance of ~100 Ω was obtained for the ZCO and GZCO samples, while the NGZCO sample had a resistance of 77 Ω, which is comparatively low relative to its counterparts. The lower charge transfer resistance helped the NGZCO maintain good capacity retention by promoting easy access for charge migration during cycling. Overall, from the discussion, it is concluded that the mesoporous $ZnCo_2O_4$/N-doped rGO composite presented in this study is a promising anode material for LIBs.

## 4. Conclusion

We have developed hydrothermal and thermal annealing process to synthesize novel mesoporous $ZnCo_2O_4$/N-doped rGO nanoarchitectures for use as high-capacity anode materials in LIBs. The strong synergy between N-doped rGO and $ZnCo_2O_4$ helped to enhance the bonding in the composite and to create a uniform dispersion of $ZnCo_2O_4$ on N-doped rGO sheets, leading to a highly conducting network system. Also, the wormhole-like structure has an exceptional ability to accommodate volume changes effectively due to its high porosity and the presence of defects in the N-doped rGO, which improve the reactivity of the $ZnCo_2O_4$ during discharge–charge reactions. Moreover, the mesoporous $ZnCo_2O_4$/N-doped rGO nanoarchitecture electrode shows enhanced reversible performances during cyclic tests, maintaining the specific capacity of 998 mAh $g^{-1}$ after 30 cycles at 0.1 A $g^{-1}$. These unique mesoporous $ZnCo_2O_4$/N-doped rGO nanostructures

show good potential for use in backbone conductive networked structures of anode materials in LIBs.

## Acknowledgements

This work was supported by Agency for Defense Development as a part of basic research program under the contract UD130049GD. This work was supported by the International Collaborative Energy Technology R&D Program of the Korea Institute of Energy Technology Evaluation and Planning (KETEP), granted financial resource from the Ministry of Trade, Industry & Energy, Republic of Korea (No. 20128510010050).

## Appendix A. Supplementary data

Supplementary data associated with this article can be found, in the online version, at http://dx.doi.org/10.1016/j.carbon.2015.07.024.

## References

[1] Y. Idota, T. Kubota, A. Matsufuji, Y. Maekawa, T. Miyasaka, Tin-based amorphous oxide: a high-capacity lithium-ion-storage material, Science 276 (5317) (1997) 1395–1397.
[2] K. Zhong, X. Xia, B. Zhang, H. Li, Z. Wang, L. Chen, MnO powder as anode active materials for lithium ion batteries, J. Power Sources 195 (10) (2010) 3300–3308.
[3] X. Yu, Y. He, J. Sun, K. Tang, H. Li, L. Chen, et al., Nanocrystalline MnO thin film anode for lithium ion batteries with low overpotential, Electrochem. Commun. 11 (4) (2009) 791–794.
[4] B. Koo, H. Xiong, M.D. Slater, V.B. Prakapenka, M. Balasubramanian, P. Podsiadlo, et al., Hollow iron oxide nanoparticles for application in lithium ion batteries, Nano Lett. 12 (5) (2012) 2429–2435.
[5] P. Poizot, S. Laruelle, S. Grugeon, L. Dupont, J. Tarascon, Nano-sized transition-metal oxides as negative-electrode materials for lithium-ion batteries, Nature 407 (6803) (2000) 496–499.
[6] F. Li, Q.-Q. Zou, Y.-Y. Xia, CoO-loaded graphitable carbon hollow spheres as anode materials for lithium-ion battery, J. Power Sources 177 (2) (2008) 546–552.
[7] H. Wang, L.-F. Cui, Y. Yang, H. Sanchez Casalongue, J.T. Robinson, Y. Liang, et al., $Mn_3O_4$–graphene hybrid as a high-capacity anode material for lithium ion batteries, J. Am. Chem. Soc. 132 (40) (2010) 13978–13980.
[8] Z.-S. Wu, W. Ren, L. Wen, L. Gao, J. Zhao, Z. Chen, et al., Graphene anchored with $Co_3O_4$ nanoparticles as anode of lithium ion batteries with enhanced reversible capacity and cyclic performance, ACS Nano 4 (6) (2010) 3187–3194.
[9] F. Lou, H. Zhou, T.D. Tran, M.E. Melandsø Buan, F. Vullum-Bruer, M. Rønning, et al., Coaxial carbon/metal oxide/aligned carbon nanotube arrays as high-performance anodes for lithium ion batteries, ChemSusChem 7 (5) (2014) 1335–1346.
[10] R. Alcántara, M. Jaraba, P. Lavela, J. Tirado, $NiCo_2O_4$ spinel: first report on a transition metal oxide for the negative electrode of sodium-ion batteries, Chem. Mater. 14 (7) (2002) 2847–2848.
[11] Y. Sharma, N. Sharma, G. Subba Rao, B. Chowdari, Studies on spinel cobaltites, $FeCo_2O_4$ and $MgCo_2O_4$ as anodes for Li-ion batteries, Solid State Ionics 179 (15) (2008) 587–597.
[12] L. Hu, B. Qu, C. Li, Y. Chen, L. Mei, D. Lei, et al., Facile synthesis of uniform mesoporous $ZnCo_2O_4$ microspheres as a high-performance anode material for Li-ion batteries, J. Mater. Chem. A 1 (18) (2013) 5596–5602.
[13] Y. Sharma, N. Sharma, G. Subba Rao, B. Chowdari, Nanophase $ZnCo_2O_4$ as a high performance anode material for Li-ion batteries, Adv. Funct. Mater. 17 (15) (2007) 2855–2861.
[14] P. Lavela, J. Tirado, C. Vidal-Abarca, Sol–gel preparation of cobalt manganese mixed oxides for their use as electrode materials in lithium cells, Electrochim. Acta 52 (28) (2007) 7986–7995.
[15] F.M. Courtel, H. Duncan, Y. Abu-Lebdeh, I.J. Davidson, High capacity anode materials for Li-ion batteries based on spinel metal oxides $AMn_2O_4$ (A= Co, Ni, and Zn), J. Mater. Chem. 21 (27) (2011) 10206–10218.
[16] Y. Yang, Y. Zhao, L. Xiao, L. Zhang, Nanocrystalline $ZnMn_2O_4$ as a novel lithium-storage material, Electrochem. Commun. 10 (8) (2008) 1117–1120.
[17] L. Hu, H. Zhong, X. Zheng, Y. Huang, P. Zhang, Q. Chen, $CoMn_2O_4$ spinel hierarchical microspheres assembled with porous nanosheets as stable anodes for lithium-ion batteries, Sci. Rep. 2 (2012).
[18] P.F. Teh, Y. Sharma, S.S. Pramana, M. Srinivasan, Nanoweb anodes composed of one-dimensional, high aspect ratio, size tunable electrospun $ZnFe_2O_4$ nanofibers for lithium ion batteries, J. Mater. Chem. 21 (38) (2011) 14999–15008.
[19] B. Liu, J. Zhang, X. Wang, G. Chen, D. Chen, C. Zhou, et al., Hierarchical three-dimensional $ZnCo_2O_4$ nanowire arrays/carbon cloth anodes for a novel class of high-performance flexible lithium-ion batteries, Nano Lett. 12 (6) (2012) 3005–3011.
[20] Z. Jin, J. Yao, C. Kittrell, J.M. Tour, Large-scale growth and characterizations of nitrogen-doped monolayer graphene sheets, ACS Nano 5 (5) (2011) 4112–4117.
[21] D. Deng, X. Pan, L. Yu, Y. Cui, Y. Jiang, J. Qi, et al., Toward N-doped graphene via solvothermal synthesis, Chem. Mater. 23 (5) (2011) 1188–1193.
[22] L. Panchakarla, K. Subrahmanyam, S. Saha, A. Govindaraj, H. Krishnamurthy, U. Waghmare, et al., Synthesis, structure, and properties of boron-and nitrogen-doped graphene, Adv. Mater. 21 (46) (2009) 4726–4730.
[23] A.L.M. Reddy, A. Srivastava, S.R. Gowda, H. Gullapalli, M. Dubey, P.M. Ajayan, Synthesis of nitrogen-doped graphene films for lithium battery application, ACS Nano 4 (11) (2010) 6337–6342.
[24] Z.-S. Wu, W. Ren, L. Xu, F. Li, H.-M. Cheng, Doped graphene sheets as anode materials with superhigh rate and large capacity for lithium ion batteries, ACS Nano 5 (7) (2011) 5463–5471.
[25] H. Wang, C. Zhang, Z. Liu, L. Wang, P. Han, H. Xu, et al., Nitrogen-doped graphene nanosheets with excellent lithium storage properties, J. Mater. Chem. 21 (14) (2011) 5430–5434.
[26] D. Li, D. Shi, Z. Liu, H. Liu, Z. Guo, $TiO_2$ nanoparticles on nitrogen-doped graphene as anode material for lithium ion batteries, J. Nanopart. Res. 15 (5) (2013) 1–10.
[27] X. Jiang, X. Yang, Y. Zhu, H. Jiang, Y. Yao, P. Zhao, et al., 3D nitrogen-doped graphene foams embedding ultrafine $TiO_2$ nanoparticles for high-performance lithium-ion batteries, J. Mater. Chem. A (2014).
[28] T. Yang, T. Qian, M. Wang, J. Liu, J. Zhou, Z. Sun, et al., A new approach towards the synthesis of nitrogen-doped graphene/$MnO_2$ hybrids for ultralong cycle-life lithium ion batteries, J. Mater. Chem. A 3 (12) (2015) 6291–6296.
[29] A.M. Cao, J.S. Hu, H.P. Liang, L.J. Wan, Self-assembled vanadium pentoxide ($V_2O_5$) hollow microspheres from nanorods and their application in lithium-ion batteries, Angew. Chem. Int. Ed. 44 (28) (2005) 4391–4395.
[30] G. Zhang, Y. Chen, B. Qu, L. Hu, L. Mei, D. Lei, et al., Synthesis of mesoporous NiO nanospheres as anode materials for lithium ion batteries, Electrochim. Acta 80 (2012) 140–147.
[31] B. Qu, M. Zhang, D. Lei, Y. Zeng, Y. Chen, L. Chen, et al., Facile solvothermal synthesis of mesoporous $Cu_2SnS_3$ spheres and their application in lithium-ion batteries, Nanoscale 3 (9) (2011) 3646–3651.
[32] S. Vijayanand, P.A. Joy, H.S. Potdar, D. Patil, P. Patil, Nanostructured spinel $ZnCo_2O_4$ for the detection of LPG, Sens. Actuators B 152 (1) (2011) 121–129.
[33] B. Varghese, C. Teo, Y. Zhu, M.V. Reddy, B.V. Chowdari, A.T.S. Wee, et al., $Co_3O_4$ nanostructures with different morphologies and their field-emission properties, Adv. Funct. Mater. 17 (12) (2007) 1932–1939.
[34] X. Wei, D. Chen, W. Tang, Preparation and characterization of the spinel oxide $ZnCo_2O_4$ obtained by sol–gel method, Mater. Chem. Phys. 103 (1) (2007) 54–58.
[35] W. Luo, X. Hu, Y. Sun, Y. Huang, Electrospun porous $ZnCo_2O_4$ nanotubes as a high-performance anode material for lithium-ion batteries, J. Mater. Chem. 22 (18) (2012) 8916–8921.
[36] G. Kustova, E. Burgina, G. Volkova, T. Yurieva, L. Plyasova, IR spectroscopic investigation of cation distribution in Zn–Co oxide catalysts with spinel type structure, J. Mol. Catal. A: Chem. 158 (1) (2000) 293–296.
[37] C.W. Na, H.-S. Woo, H.-J. Kim, U. Jeong, J.-H. Chung, J.-H. Lee, Controlled transformation of ZnO nanobelts into CoO/$Co_3O_4$ nanowires, CrystEngComm 14 (10) (2012) 3737–3741.
[38] X. Wang, J. Xu, X. Yu, K. Xue, J. Yu, X. Zhao, Structural evidence of secondary phase segregation from the Raman vibrational modes in $Zn_{1-x}Co_xO$ ($0 < x < 0.6$), Appl. Phys. Lett. 91 (3) (2007) 031908.
[39] O. Akhavan, E. Ghaderi, S. Aghayee, Y. Fereydooni, A. Talebi, The use of a glucose-reduced graphene oxide suspension for photothermal cancer therapy, J. Mater. Chem. 22 (27) (2012) 13773–13781.
[40] H. Zhang, S. Chen, X. Quan, H. Yu, H. Zhao, In situ controllable growth of noble metal nanodot on graphene sheet, J. Mater. Chem. 21 (34) (2011) 12986–12990.
[41] R. Lv, Q. Li, A.R. Botello-Méndez, T. Hayashi, B. Wang, A. Berkdemir, et al., Nitrogen-doped graphene: beyond single substitution and enhanced molecular sensing, Sci. Rep. 2 (2012).
[42] H. Chen, M.B. Müller, K.J. Gilmore, G.G. Wallace, D. Li, Mechanically strong, electrically conductive, and biocompatible graphene paper, Adv. Mater. 20 (18) (2008) 3557–3561.
[43] N. Du, Y.F. Xu, H. Zhang, J.X. Yu, C.X. Zhai, D.R. Yang, Porous $ZnCo_2O_4$ nanowires synthesis via sacrificial templates: high-performance anode materials of Li-ion batteries, Inorg. Chem. 50 (8) (2011) 3320–3324.
[44] M.V. Reddy, K.Y.H. Kenrick, T.Y. Wei, G.Y. Chong, G.H. Leong, B.V.R. Chowdari, Nano-$ZnCo_2O_4$ material preparation by molten salt method and its electrochemical properties for lithium batteries, J. Electrochem. Soc. 158 (12) (2011). A1423–A30.
[45] A.J. Smith, J.C. Burns, S. Trussler, J.R. Dahn, Precision measurements of the coulombic efficiency of lithium-ion batteries and of electrode materials for lithium-ion batteries, J. Electrochem. Soc. 157 (2) (2010) A196–A202.